

# Irradiation-Induced Extremes Create Hierarchical Face-/Body-Centered-Cubic Phases in Nanostructured High Entropy Alloys

Li Jiang, Yong-Jie Hu, Kai Sun, Pengyuan Xiu, Miao Song, Yanwen Zhang, Walker L. Boldman, Miguel L. Crespillo, Philip D. Rack, Liang Qi, William J. Weber, and Lumin Wang\*

A nanoscale hierarchical dual-phase structure is reported to form in a nanocrystalline NiFeCoCrCu high-entropy-alloy (HEA) film via ion irradiation. Under the extreme energy deposition and consequent thermal energy dissipation induced by energetic particles, a fundamentally new phenomenon is revealed, in which the original single-phase face-centered-cubic (FCC) structure partially transforms into alternating nanometer layers of a body-centered-cubic (BCC) structure. The orientation relationship follows the Nishiyama–Wasserman relationship, that is,  $(011)_{\text{BCC}} \parallel (\bar{1}\bar{1}\bar{1})_{\text{FCC}}$  and  $[100]_{\text{BCC}} \parallel [\bar{1}\bar{1}0]_{\text{FCC}}$ . Simulation results indicate that Cr, as a BCC stabilizing element, exhibits a tendency to segregate to the stacking faults (SFs). Furthermore, the high densities of SFs and twin boundaries in each nanocrystalline grain serve to accelerate the nucleation and growth of the BCC phase during irradiation. By adjusting the irradiation parameters, desired thicknesses of the FCC and BCC phases in the laminates can be achieved. This work demonstrates the controlled formation of an attractive dual-phase nanolaminate structure under ion irradiation and provides a strategy for designing new derivative structures of HEAs.

A new alloy design strategy based on hierarchical structures has demonstrated great advantages in simultaneously improving the strength, ductility, and toughness of metal alloys.<sup>[1–3]</sup> Typically, such hierarchical laminate structures are composed of a soft parent phase to improve ductility and a hard second phase that impedes dislocation motion to strengthen the alloy.<sup>[4]</sup> The interfaces dispersed in the laminate structure serve to decelerate fatigue crack propagation by deflecting the crack propagation path.<sup>[5,6]</sup> In the best-case scenario, tuning of the phase thickness or the ratio of the phases in the laminates leads to desired properties, which enables an immense variability in properties and sheds light on a new method for designing advanced engineering materials.

In recent years, multicomponent alloys or high entropy alloys (HEAs) have received increasing attention because of their attractive structures and excellent

properties.<sup>[7–10]</sup> These alloys typically contain five or more principal elements in near-equiatom concentrations and usually display a simple solid solution structure with high configurational entropy.<sup>[11–13]</sup> The metastable microstructures resulting from considerable local lattice distortions demonstrate a high potential for creating new phases under specific environments.<sup>[14,15]</sup> A load-driven phase transformation from a face-centered cubic (FCC) matrix to a hexagonal-close-packed (HCP) nanolaminate structure was reported in a CoCrFeMnNi HEA system.<sup>[2,4,16]</sup> Actually, such pressure-induced phase transformations have been observed in several HEAs under different critical pressures depending on the alloy compositions.<sup>[17–22]</sup> A magnetically-driven phase transformation from FCC to HCP was also found in a CoCrNi system.<sup>[23]</sup> Furthermore, temperature variations can also induce phase transformations in HEAs. For example, the disordered body-centered-cubic (BCC) phase in the  $\text{Al}_x\text{CoCrFeNi}$  HEA gradually transforms to an ordered B2 phase with decreasing temperature from 1200 °C.<sup>[24]</sup> Nonetheless, apart from the complex phase transformation involving intermetallics, the most common phase transformations have been observed between FCC and HCP phases. A simple difference in the stacking sequence of close-packed planes promotes reciprocal transformations through small atomic displacements.

Dr. L. Jiang, P. Xiu, Dr. M. Song, Prof. L. Wang  
Department of Nuclear Engineering and Radiological Sciences  
University of Michigan  
Ann Arbor, MI 48109, USA  
E-mail: lmwang@umich.edu


Dr. Y.-J. Hu, Dr. K. Sun, Prof. L. Qi, Prof. L. Wang  
Department of Materials Science and Engineering  
University of Michigan  
Ann Arbor, MI 48109, USA

Prof. Y. Zhang, W. L. Boldman, Prof. M. L. Crespillo, Prof. P. D. Rack,  
Prof. W. J. Weber

Department of Materials Science and Engineering  
University of Tennessee  
Knoxville, TN 37996, USA

Prof. Y. Zhang, Prof. W. J. Weber  
Materials Science and Technology Division  
Oak Ridge National Laboratory  
Oak Ridge, TN 37831, USA

Prof. P. D. Rack  
Center for Nanophase Materials Sciences  
Oak Ridge National Laboratory  
Oak Ridge, TN 37831, USA

 The ORCID identification number(s) for the author(s) of this article can be found under <https://doi.org/10.1002/adma.202002652>.

DOI: 10.1002/adma.202002652

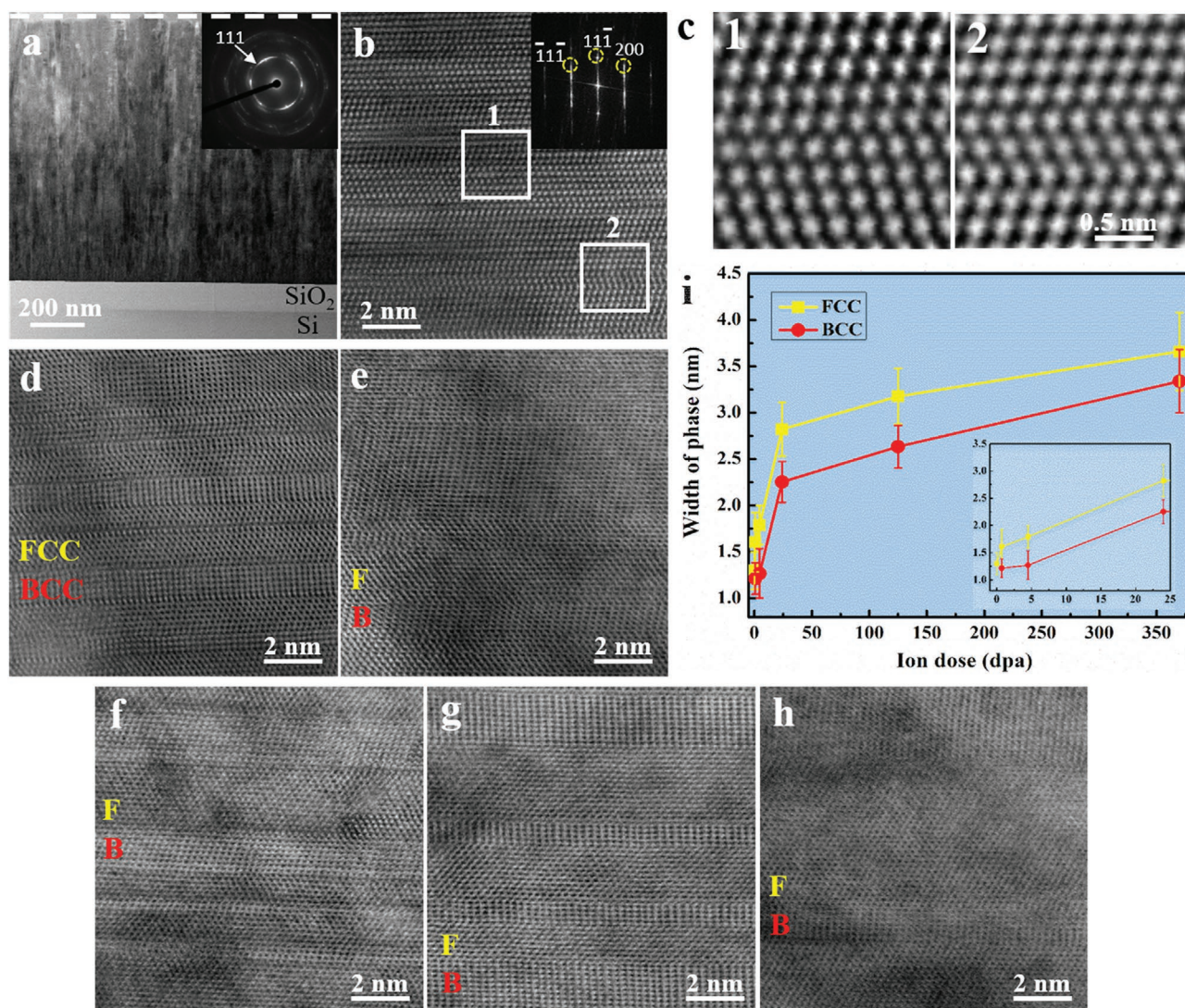


**Figure 1.** Microstructures of the as-deposited and irradiated NiFeCoCrCu films. a) Cross-sectional TEM micrograph and SAED pattern of the as-deposited film. b) HRTEM image and corresponding FFT pattern of the as-deposited film. c) IFFT images corresponding to the framed areas in (b), showing the configurations of the nanotwin and stacking fault, respectively. d–h) HRTEM images of the irradiated films with ion doses of 0.7, 4.5, 24, 125, and 370 dpa, respectively. F and B in (e–h) denote FCC and BCC, respectively. i) Evolution of widths for both FCC and BCC phases with increasing ion dose. The widths of both phases increase linearly up to 24 dpa and then display a slower increasing slope. (For interpretation of the references to color in this figure legend, the reader is referred to the web version of this article.)

In this paper, we report the formation of a hierarchical dual-phase nanolaminate structure composed of FCC and BCC phases in an initially FCC nanocrystalline NiFeCoCrCu film under 3 MeV Ni ion irradiation. Ion-induced displacement cascades can create high transient temperatures (several thousand Kelvin) and high-pressure waves (10–50 GPa) within short distances (<2 Å).<sup>[25,26]</sup> Under such extreme conditions, the original single-phase FCC structure partially transforms to a BCC structure, resulting in a nanolaminate structure with alternating BCC and FCC phases. The orientation relationship of the FCC and BCC phases follows the Nishiyama–Wassermann (N–W) relationship, that is,  $(011)_{\text{BCC}} \parallel (\bar{1}\bar{1}\bar{1})_{\text{FCC}}$  and  $[100]_{\text{BCC}} \parallel [1\bar{1}0]_{\text{FCC}}$ . With increasing ion irradiation dose, the thicknesses of the FCC and BCC phases in the laminate structure change correspondingly, thus achieving tailored mixtures of hard BCC and

ductile FCC phases, while optimizing the number of the phase boundaries within each nanocrystalline grain.

Detailed microstructural characterization of the as-deposited NiFeCoCrCu film using transmission electron microscopy (TEM) reveals a film thickness of 1 μm on a Si substrate with a native SiO<sub>2</sub> layer. Generally, a large number of columnar grains with growth direction perpendicular to the HEA/SiO<sub>2</sub> interface are observed. The selected-area electron diffraction (SAED) pattern inserted in **Figure 1a** indicates an FCC crystal structure texture along the  $\langle 111 \rangle$  direction. These columnar grains, containing a high density of nanotwins, display an average width of around 10 nm, with most growth-twin planes parallel to the film surface (Figure 1b). The  $\{111\}$  diffraction spot splitting in the fast Fourier transform (FFT) image converted from Figure 1b is consistent with the  $\{111\}$  twins. The inverse FFT (IFFT) images

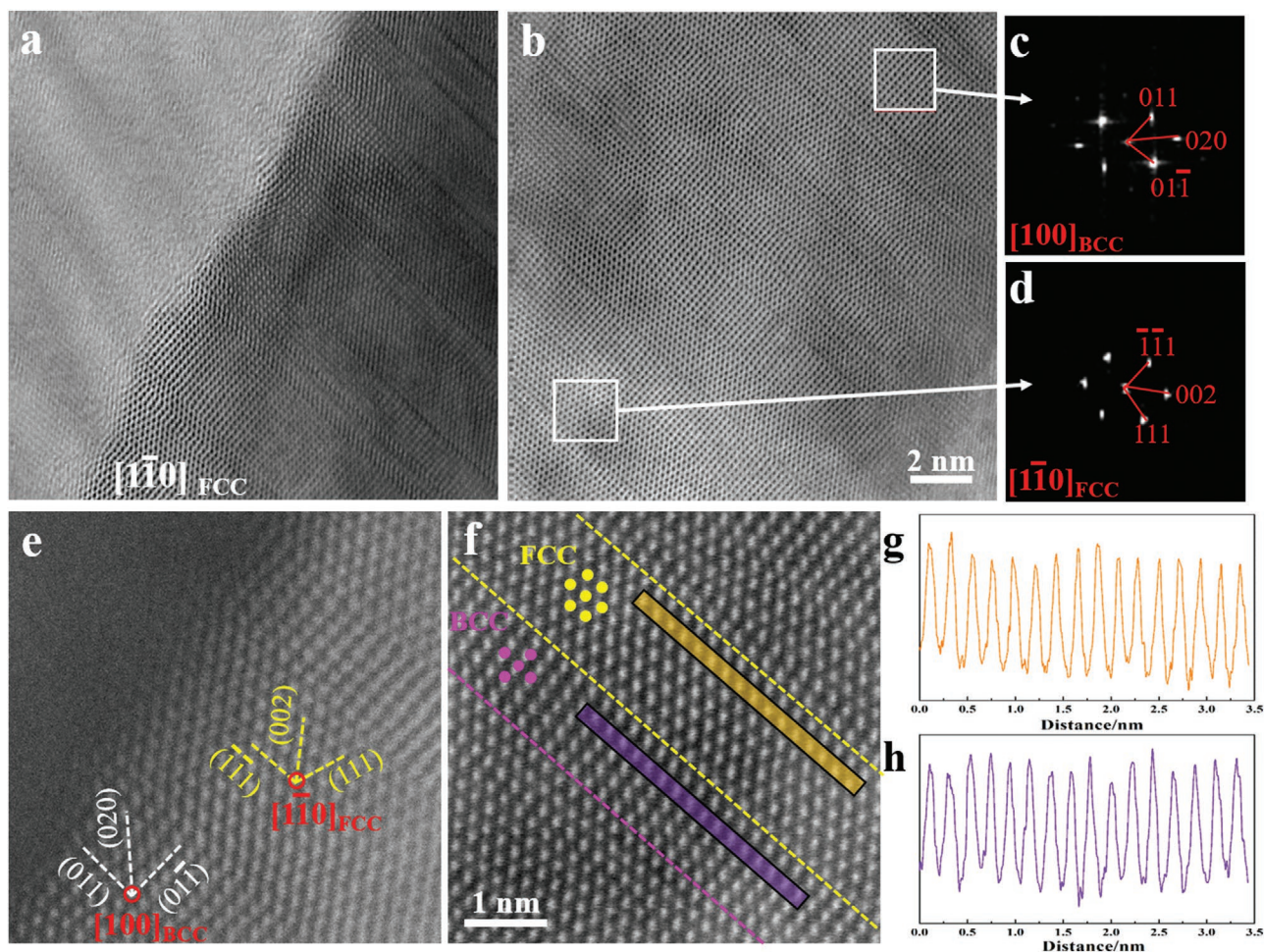


**Figure 2.** Microstructures of the NiFeCoCrCu film irradiated to 0.7 dpa. a,b) BF images, displaying two alternating crystal lattices exist in the same crystalline grain (b) and eventually terminating at the edge of the grain boundary (a). Images (a) and (b) share the same scale bar. c,d) The FFT patterns converted from the framed areas in (b), suggesting the BCC and FCC crystal structures respectively. e,f) HAADF images, showing detailed orientation relationship of the FCC and BCC crystal lattices. Images (e) and (f) share the same scale bar. g,h) The contrast profiles along the yellow (g) and purple (h) lines, which indicate the interplanar spacings are 2.0 and 1.95 Å, respectively.

(Figure 1c) of the framed areas in Figure 1b exhibit a typical nanotwin and a stacking fault (SF). Moreover, statistical measurements of ten crystalline grains indicate that the average twinning thickness is 1.3 nm, and the average spacing between adjacent twins is on the same scale.

The irradiation direction is perpendicular to the film surface, as indicated by the dotted line in Figure 1a. The analyzed regions for each sample are around 400–600 nm below the surface, corresponding to average damage doses of 0.7, 4.5, 24, 125, and 370 displacement per atom (dpa) respectively. For all the irradiated films, new crystal lattices with a different orientation (confirmed to be BCC below) interspersed with the original FCC crystal lattices are identified in the high-resolution TEM (HRTEM) images in Figure 1d–h. At least ten areas for each sample have been investigated by TEM to confirm the homogeneity of the phase transformation. The average widths of both the FCC and BCC phases in each sample were measured from ten individual crystalline grains, and the results with the standard deviation are shown in Figure 1i, which indicate a linear increase in widths up to 24 dpa and a slower growth with

further increases in dose. Irradiation-induced growth of the twins in nanotwinned Cu and nanotwinned Ag has been previously reported.<sup>[27–29]</sup> These researchers concluded that the twins grow through a detwinning mechanism during irradiation, with a driving force related to the reduction of twin boundary energy.<sup>[30]</sup> Similarly, the irradiation-induced phase growth in our study is dominated mainly by the reduction of the phase boundary energy, the rapid energy release at the initial stage promotes the linear growth of both phases.

To determine the orientation of the dual-phase microstructure, detailed TEM analysis was performed on the HEA film irradiated to 0.7 dpa. From the bright-field (BF) TEM images, two alternating crystal lattices exist in the grain interior, which eventually terminate at the grain boundaries (GBs) (Figure 2a,b). Figure 2a and e reveal the details of the GB structures, showing that when the crystalline grain on the right side is tilted on-zone, the grain on the left is far from the on-zone orientation, indicating a large-angle twist feature of the GBs. In addition, transmission Kikuchi Diffraction (TKD) results reveal that the average twist angle of the GBs between adjacent

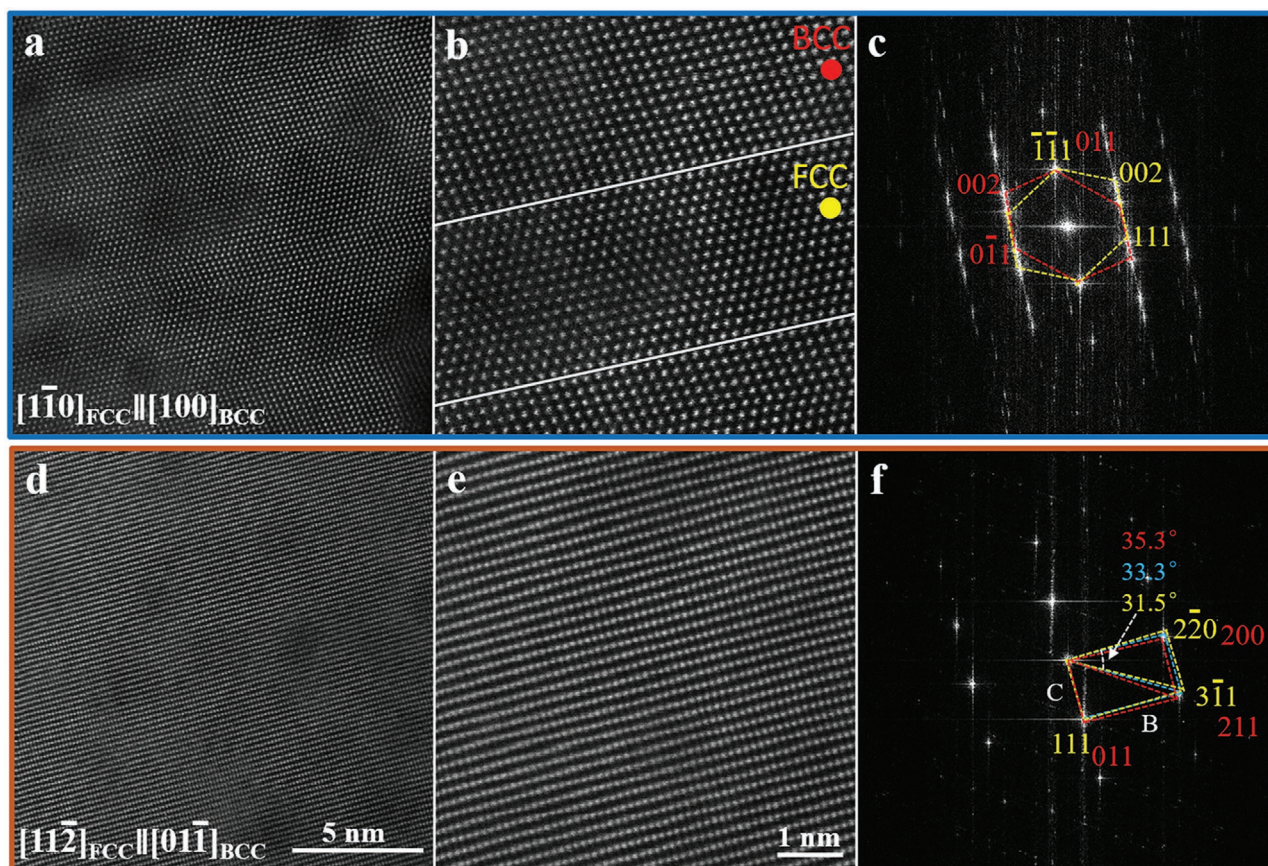


**Figure 3.** HAADF images and FFT patterns of the NiFeCoCrCu film irradiated to 370 dpa. a–c) From the  $[1\bar{1}0]_{\text{FCC}}$  on-zone condition. The crystallographic orientation relationship follows  $(011)_{\text{BCC}} \parallel (\bar{1}\bar{1}1)_{\text{FCC}}$  and  $[100]_{\text{BCC}} \parallel [1\bar{1}0]_{\text{FCC}}$ . d–f) From the  $[11\bar{2}]_{\text{FCC}}$  on-zone condition, which verify the orientation relationship of  $[11\bar{2}]_{\text{FCC}} \parallel [01\bar{1}]_{\text{BCC}}$ . Images (a) and (d) share the same scale bar; images (b) and (e) share the same scale bar. The blue frame in (f) represents the actual FFT pattern, while the red and yellow frames represent the theoretical FFT patterns of the BCC and FCC phases, respectively.

parallel grains is around  $45^\circ$ , indicating the large-angle nature of the GBs (Figures S1 and S2, Supporting information). The crystallographic analysis, based on the FFT patterns converted from the framed areas in Figure 2b, suggests that the bottom framed area still depicts an FCC crystal structure, whereas the top framed area corresponds to a BCC structure (Figure 2c,d). Further, the BCC lattice planes have a consistent orientation relationship with the matrix grain, with  $(\bar{1}\bar{1}1)_{\text{FCC}} \parallel (011)_{\text{BCC}}$  and  $[1\bar{1}0]_{\text{FCC}} \parallel [100]_{\text{BCC}}$ ; at the same time, the BCC lattice planes share the same  $\{111\}$  habit planes as the coherent boundaries of the FCC phases, as shown in the high angle annular dark field (HAADF) images in Figure 2e,f. By measuring the intensity profiles (Figure 2g,h) along both the  $(\bar{1}\bar{1}1)_{\text{FCC}}$  atomic columns (colored in orange) and the  $(011)_{\text{BCC}}$  atomic columns (colored in purple) in Figure 2f, the interplanar spacings of the  $(\bar{1}\bar{1}1)_{\text{FCC}}$  and  $(011)_{\text{BCC}}$  are determined to be 2.0 Å and 1.95 Å, respectively. Accordingly, the lattice parameters of the FCC and BCC structures are calculated to be 3.50 and 2.76 Å, respectively.

**Figure 3** displays the HAADF images of the HEA film after irradiation to a damage dose of 370 dpa. The images taken from  $[1\bar{1}0]_{\text{FCC}}$  zone axis, as well as the corresponding FFT pattern (Figure 3a–c), demonstrate a more significant lattice distortion compared with the relatively ordered configuration in the film irradiated to 0.7 dpa. However, the orientation relationship is

consistent with that observed in films irradiated at low damage doses, that is,  $(\bar{1}\bar{1}1)_{\text{FCC}} \parallel (011)_{\text{BCC}}$  and  $[1\bar{1}0]_{\text{FCC}} \parallel [100]_{\text{BCC}}$ . Further, the same areas were tilted to the  $[11\bar{2}]_{\text{FCC}}$  zone axis for verification of the above conclusion (Figure 3d–f). It is noted that no obvious differences in the lattice arrangements exist between the two phases from this orientation. Based on the crystallographic indexing, the  $[01\bar{1}]_{\text{BCC}}$  zone axis of the BCC phase is parallel to the  $[11\bar{2}]_{\text{FCC}}$  zone axis of the FCC phase; and the FFT pattern of the  $(2\bar{2}0)_{\text{FCC}}$  is likely to overlap with the  $(200)_{\text{BCC}}$ , while the  $(111)_{\text{FCC}}$  overlaps with the  $(011)_{\text{BCC}}$ . Indeed, the actual vertex angle of the triangle measured from the FFT pattern is  $33.3^\circ$ , and the ratio of B to C is 1.55 (B and C represent the magnitude of relevant reciprocal lattice vectors indicated in the FFT pattern), as framed by blue dotted lines in Figure 3f. Similarly, the theoretical vertex angle and B/C are  $31.5^\circ$  and 1.63 for the FCC phase, and  $35.3^\circ$  and 1.41 for the BCC phase, which are framed by yellow and red dotted lines, respectively. It is thought that the actual FFT pattern exists between the theoretical patterns of the FCC and BCC phases. Considering the significant lattice distortion in the high ion dose irradiated HEA film, it is expected that the crystal lattices of the adjacent phases tend to deform toward each other to decrease the systematic energy during irradiation, leading to the approach and even overlap of the FFT patterns of the FCC

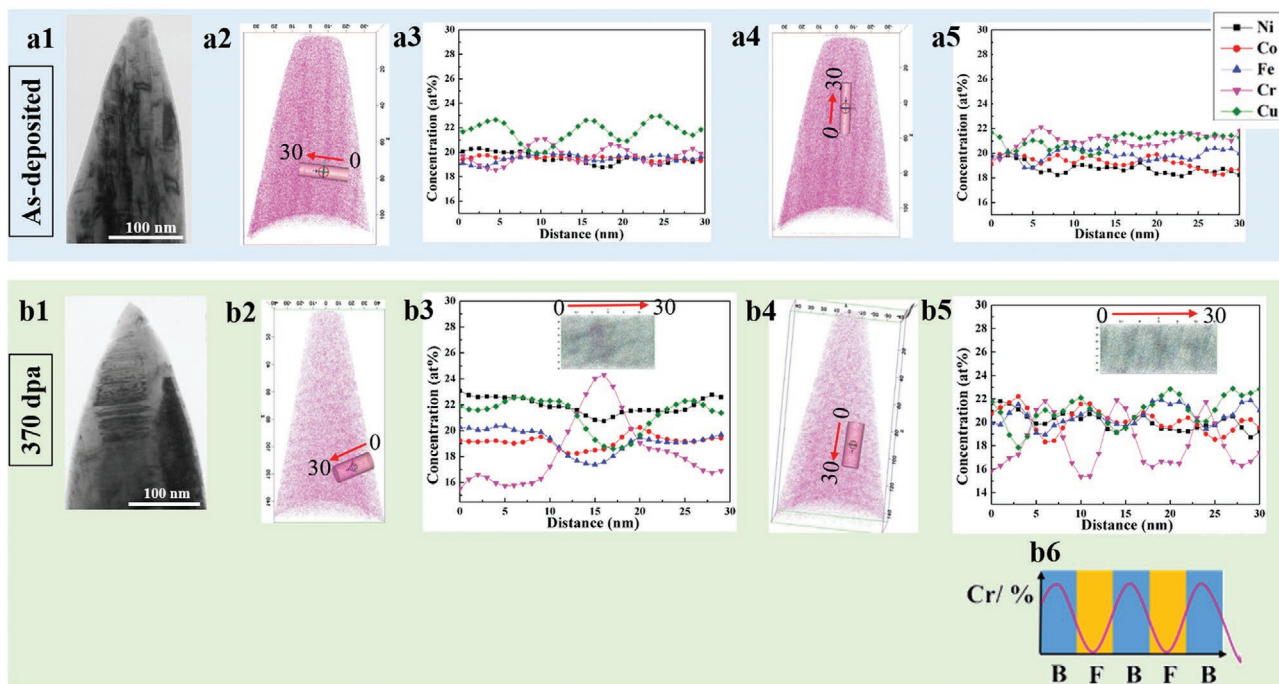


**Figure 4.** Correlative TEM and APT results from the as-deposited film and the film irradiated to 370 dpa. a1) TEM image of the atom probe tip of the as-deposited film, showing several directional columnar grains with detectable GBs. a2,a3) Analytical cylinder and 1D concentration profile across the GBs. The GBs are rich in Cu and depleted of Cr. a4,a5) Analytical cylinder and 1D concentration profile in the grain interior. All the elements distribute homogeneously. b1) TEM image of the atom probe tip of the film irradiated to 370 dpa, showing a GB and the lamellar structures in the grain interior. b2,b3) Analytical cylinder and 1D concentration profile across the GB. Cr segregates to the GB. b4,b5) Analytical cylinder and 1D concentration profile in the grain interior. An obvious wavy distribution of Cr is observed. b6) Schematic diagram showing the distribution of Cr in the FCC (F) and BCC (B) phases, respectively, in the film irradiated to 370 dpa.

and the BCC phases from the  $[11\bar{2}]_{\text{FCC}}/[01\bar{1}]_{\text{BCC}}$  direction. Thus, the orientation relationship of the dual-phase microstructure in the irradiated NiFeCoCrCu films is further revealed to follow the N–W relationship.

Radiation-induced elemental segregation at GBs and within grain interiors was characterized using correlative TEM and atom probe tomography (APT) to accurately relate the crystallographic features to the chemical information. From the tip image of the as-deposited film, several directional columnar grains with detectable GBs are observed (Figure 4a1). The typical 1D composition profile across three GBs using an analytical cylinder with a diameter of 10 nm is shown in Figure 4a3. Comparison with the TEM micrograph makes it apparent that the GBs are rich in Cu and depleted in Cr, while containing equal amounts of the other three elements. Meanwhile, the 1D concentration profile inside a columnar grain indicates a homogeneous elemental distribution (Figure 4a5), which is consistent with the previously reported as-cast bulk NiFeCoCrCu.<sup>[31]</sup>

For the film irradiated to 370 dpa, only one GB is observed in the atom probe tip (Figure 4b1). The decreasing density of the GBs is attributed to irradiation-induced grain growth.<sup>[32,33]</sup> From the 1D concentration profile across the GB, significant elemental redistribution is observed that indicates a peak distribution of Cr at the GB. The wavy distribution of Cr inside the columnar grains is also pronounced (Figure 4b5), the combination of the microstructural analysis inside the crystalline grains suggests that it may be induced by the compositional

differences between the adjacent FCC and BCC phases. However, similar structural features in the adjacent phases reveal challenges to correlate microstructures and compositions. Energy-dispersive X-ray spectrometry (EDS) results indicate an enrichment of Cr in the BCC phase and a relative depletion of Cr in the FCC phase (Figure S3, Supporting information), which verifies that Cr content differences in adjacent FCC and BCC phases lead to its wavy distribution in the APT results. Further, the symmetric distribution of Cr concentration in the BCC phase indicates that Cr diffuses to the twin boundary from both sides. Moreover, it is worth noting that the widths of the Cr enriched areas in Figure 4b correspond well with the phase widths in the TEM results. The distance between the adjacent valleys (around 6 nm) represents the combined width of a FCC/BCC phase couple (Figure 4b6), which is consistent with the TEM results that the respective widths of the FCC and BCC phases are both around 3 nm after irradiation to 370 dpa.

Previous studies have demonstrated that ion irradiation could induce phase transformation or amorphization in materials, especially for thin film samples. The release of the complex residual stress during or after irradiation serves to stimulate structural transformations. The phase transformation from FCC to HCP, which has been observed in Co-based films irradiated with 15 MeV Au ions, is induced by the local energy dissipation along the track of the ion beam.<sup>[34]</sup> A martensite transformation has been observed in TiNi films under 350 kV electron irradiation and is induced by the chain displacement of atoms from their lattice sites by energetic electrons.<sup>[35]</sup> Some

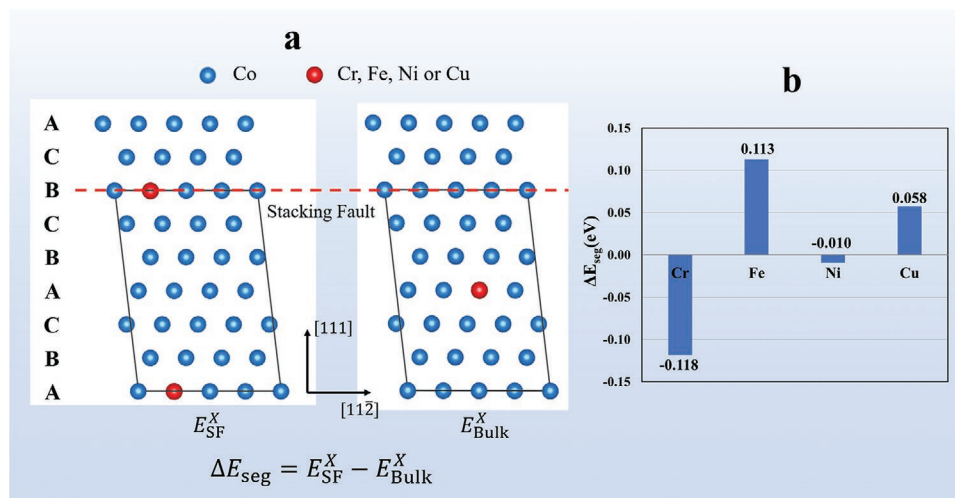


**Figure 5.** a) Schematic diagrams of the atomic arrangement, showing a SF in the absence of an A stacking atomic layer. In this simulation, Co metal is used to represent the quinary NiFeCoCrCu, since the VEC value of Co is close to the average value of the NiFeCoCrCu, which could better reflect the average level of the atomic interactions in the quinary HEA. The positions of Cr, Fe, Ni, or Cu atoms on the SF and in the bulk interior are shown in red. b) The energy difference of a Cr, Fe, Ni, or Cu atom on the SF and in the bulk interior ( $\Delta E_{\text{seg}} = E_{\text{SF}}^X - E_{\text{Bulk}}^X$ ). The segregation tendency of each element to the SF shows a decreasing sequence of  $\text{Cr} > \text{Ni} > \text{Cu} > \text{Fe}$ .

previous studies have claimed that elemental segregation could activate phase transformations, for example, the depletion of Ni in 304L steel during irradiation tends to cause a phase transformation from austenite to ferrite, since Ni is a potent austenite stabilizer.<sup>[36]</sup> A martensite to austenite transformation has been reported in Fe–Cr–C steel induced by the segregation of C at the martensite-martensite GBs.<sup>[37]</sup>

Based on the TEM and APT results in this study, the single FCC phase with a high density of nanotwins partially transforms to a BCC phase in response to ion irradiation. Irradiation does not cause an overall phase transformation in the NiFeCoCrCu film, but it leads to the formation of a nanoscale hierarchical structure composed of FCC and BCC phases. Assuming the phase transformation is caused by shear stress accompanying displacement cascades, the collective atom displacements would result in the formation of a new phase within a large area instead of the current nanoscale dual-phase laminate structure.

From the perspective of phase transformation kinetics, the origin of the new phase is generally considered to stem from heterogeneous nucleation. Various lattice defects, such as surfaces and GBs, are favorable for new phase nucleation.<sup>[38,39]</sup> Furthermore, defects that induce a larger local stress will exhibit a higher probability for providing nucleation sites.<sup>[40,41]</sup> For a symmetric, low-angle tilt GB, the nucleation is likely to be delayed, as the stresses around this GB are diminished under the interaction of constituent dislocations. In the HRTEM results and the TKD results discussed above, the GBs in the current nanocrystalline HEA film display a large-angle twist feature that effectively serves as a new phase nucleation site during irradiation. Further, the high densities of SFs and nanotwin boundaries in the grain interior also demonstrate advantages for the nucleation of new phases.

By considering the homogeneous elemental distribution of the as-deposited film and the enrichment of Cr in the BCC phase after irradiation, the possible chemical driving forces for the FCC to BCC phase transformation have been investigated.

First, the segregation energy of each element from the bulk interior to a SF has been calculated by first-principles calculations based on density functional theory (DFT) using the equation  $\Delta E_{\text{seg}} = E_{\text{SF}}^X - E_{\text{Bulk}}^X$ , where  $E_{\text{SF}}^X$  and  $E_{\text{Bulk}}^X$  are the total energies of the supercell with a solute atom  $x$  on the SF and in the bulk matrix, respectively. Therefore, a negative value of  $\Delta E_{\text{seg}}$  indicates an attractive segregation tendency. In this simulation, Co metal is used to represent the quinary NiFeCoCrCu, since the valence electron concentration (VEC) of Co is close to the average value of the NiFeCoCrCu. Thus, it is assumed that pure Co would better reflect the average level of the atomic interactions in the quinary HEA. From **Figure 5a,b**, the segregation tendency shows a decreasing sequence of  $\text{Cr} > \text{Ni} > \text{Cu} > \text{Fe}$ ; consequently, Cr exhibits the greatest tendency to segregate toward the SF of all the elements. As a BCC stabilizing element, the segregation of Cr would promote the nucleation and growth of the BCC phase at SFs, as well as at nanotwin boundaries with atomistic structures similar to the SFs, while leaving the initial FCC structure depleted in Cr. The high densities of SFs and twin boundaries in each nanocrystalline grain could explain the nanoscale hierarchical dual-phase structure in the NiFeCoCrCu film. Notably, both the kinetic and thermodynamic conditions for the phase transformation are indispensable under the irradiation condition used.

Similarly, the N–W orientation relationship of the FCC and BCC phases in this study has been previously observed in Fe–Mn steel and reportedly induced by diffusional epitaxial growth of the austenite to martensite transformation.<sup>[42,43]</sup> For the current NiFeCoCrCu, the high densities of SFs and twin boundaries serve to decrease the atomic diffusion paths that activate the nucleation and growth of the new phase under irradiation, even at low ion doses. Therefore, the phase transformation from FCC to BCC in the NiFeCoCrCu nanocrystalline film under irradiation is favored by both kinetics and thermodynamics.

In summary, a nanoscale FCC to BCC phase transformation is achieved in a nanocrystalline NiFeCoCrCu film under

high temperatures (several thousand kelvin) and high-pressure waves (10–50 GPa) induced by ion irradiation. An attractive hierarchical dual-phase structure with a tunable mixture of hard BCC and ductile FCC phases provides the possibility to tailor alloy properties without changing the composition. However, the phase stability of the present irradiated HEA films at high temperature deserves to be further investigated in the future. This work not only broadens the perception of irradiation effects in nanocrystalline films but also provides a new strategy for tailoring material structures on the nanometer or sub-nanometer scales.

## Experimental Section

The high entropy NiFeCoCrCu thin films of  $\approx 1 \mu\text{m}$  thickness were deposited on (001) Si substrates with a 5 nm buffer layer of SiO<sub>2</sub> using a direct current magnetron sputtering system. The deposition process was described in ref. [44].

These NiFeCoCrCu films were irradiated at room temperature using 3 MeV Ni<sup>+</sup> (self-ions) along the growth direction of the crystalline grains to five different fluences of  $4.7 \times 10^{14}$ ,  $2.8 \times 10^{15}$ ,  $1.5 \times 10^{16}$ ,  $8.0 \times 10^{16}$ , and  $2.4 \times 10^{17}$  ions cm<sup>-2</sup>. The irradiations were carried out using the 3.0 MV tandem accelerator facility at the Ion Beam Materials Laboratory located at the University of Tennessee.<sup>[45]</sup> Beam homogeneity was verified by ion-induced luminescence from silica targets mounted below the samples and was found to be within 10% throughout the irradiated area. The flux was controlled at  $6.94 \times 10^{12}$  ions·cm<sup>-2</sup>·s<sup>-1</sup>. The low beam current density employed reduced any undesired heating effects and charge accumulation on the samples during irradiation. Displaced atom profiles and energy deposition profiles were calculated using SRIM 2013 software in a full-cascade mode to estimate the damage dose in displacements per atom (Figure S4, Supporting information), assuming a film density of 8.356 g·cm<sup>-3</sup> with a threshold displacement energy of 40 eV for all the constituent elements.<sup>[46]</sup> The theoretical density of the solid-solution alloy was roughly estimated from the atomic fraction, atomic weight, and density of each constituent element. Regions at a depth of around 500 nm were chosen for microstructural characterization, and the average damage dose at this depth was 0.7, 4.5, 24, 125, and 370 dpa, respectively, for the ion fluences in this study.

Cross-sectional TEM foils from irradiated samples were prepared by a focused ion beam (FIB) lift-out technique using a FEI Helios Nanolab dual beam workstation at the Michigan Center for Material Characterization at the University of Michigan. A flash polishing technique was applied to each sample to remove FIB damage. A double Cs-corrected JEOL 3100R05 microscope operated at 300 keV was employed for microstructural analysis. TKD was also conducted with Helios using an accelerating voltage of 30 keV and a step size of 1 nm.

APT specimens before and after irradiation were prepared by FIB lift-out. A final 2 kV mill was applied to remove the remaining Pt protective layer, as well as the residual Ga damaged layer. Before APT characterization, the microstructures in the tips were analyzed by TEM using a JEOL 3100R05 microscope. The tips were then moved to a Cameca puck specimen assembly for APT tests. APT characterizations were conducted on a LEAP 5000X HR instrument (Cameca) at a base temperature of 40 K, operated in laser-pulsed mode (wavelength 355 nm; pulse repetition rate: 200 kHz) with 0.4 nJ pulse energy. The Imago Visualization and Analysis software version 3.8 was used to perform 1D and 3D reconstruction and composition analysis. The correlative TEM and APT technique clearly revealed the positions of the GBs and the corresponding elemental distribution.

To simulate the SF structures, a 48-atom supercell containing six (111)-layers was used. Based on the lattice parameter of FCC Co ( $a_0$ ), an orthorhombic supercell was constructed with a geometry of  $[112]a_0 \times [1\bar{1}0]a_0 \times 2[111]a_0$  in the lattice indices of the conventional FCC cell. A shear of  $\frac{1}{6}[11\bar{2}]a_0$  was applied to the lattice vectors of the

orthorhombic supercell along the  $x$  direction, and the atomic positions were kept unchanged in Cartesian coordinates to generate a SF between the (111) layers on the top and bottom of the supercell. To investigate the segregation tendency of Cr, Fe, Ni, and Cu, one Co atom was substituted by a solute atom, as shown in Figure 5a. The segregation energy was defined as  $\Delta E_{\text{seg}} = E_{\text{SF}}^x - E_{\text{Bulk}}^x$ , where  $E_{\text{SF}}^x$  and  $E_{\text{Bulk}}^x$  are the total energies of the supercell with a solute atom  $x$  on the SF and in the bulk matrix, respectively. Therefore, a more negative value of  $\Delta E_{\text{seg}}$  corresponds to a stronger segregation tendency. The first-principles calculations in the current work were performed using the Vienna Ab-initio Simulation Package (VASP).<sup>[47]</sup> The projector augmented wave method,<sup>[48]</sup> and the exchange-correlation function depicted by the general gradient approximation from Perdew, Burke, and Ernzerhof were employed.<sup>[49]</sup> The energy cutoff of the plane wave was set at 350 eV. Brillouin zone integration was performed using a first-order Methfessel-Paxton smearing of 0.2 eV.<sup>[50]</sup> According to the size and geometry of the simulation supercells, the grid for the  $k$ -point mesh was set as  $5 \times 8 \times 3$ . The energy convergence criterion of the electronic self-consistency was set at  $10^{-6}$  eV. Co-linear spin alignment (ISPIN = 2) was enabled in all the calculations. The initial magnetic states of the input atomic configurations were set to be ferrimagnetic.

## Supporting Information

Supporting Information is available from the Wiley Online Library or from the author.

## Acknowledgements

This work was supported as part of the Energy Dissipation to Defect Evolution (EDDE) Center, an Energy Frontier Research Center funded by the US Department of Energy, Office of Science, Basic Energy Sciences under contract number DE-AC05-00OR22725. Ion beam work was performed at the UT ORNL Ion Beam Materials Laboratory located on the campus of the University of Tennessee-Knoxville. Cross-sectional TEM was conducted in the Michigan Center for Material Characterization of the University of Michigan. The authors acknowledge support from the Center for Nanophase Materials Sciences, a DOE Office of Science User Facility.

## Conflict of Interest

The authors declare no conflict of interest.

## Keywords

dual phase, hierarchical structures, high entropy alloys, ion irradiation, phase transformation

Received: April 18, 2020

Revised: July 12, 2020

Published online: August 20, 2020

[1] E. Ma, T. Zhu, *Mater. Today* **2017**, *20*, 323.

[2] Z. Li, K. G. Pradeep, Y. Deng, D. Raabe, C. C. Tasan, *Nature* **2016**, *534*, 227.

[3] J. Su, D. Raabe, Z. Li, *Acta Mater.* **2019**, *163*, 40.

[4] W. Lu, C. H. Liebscher, G. Dehm, D. Raabe, Z. Li, *Adv. Mater.* **2018**, *30*, 1804722.

- [5] M. Koyama, Z. Zhang, M. M. Wang, D. Ponge, D. Raabe, K. Tsuzaki, H. Noguchi, C. C. Tasan, *Science* **2017**, 355, 1055.
- [6] Y. Lu, X. Gao, L. Jiang, Z. Chen, T. Wang, J. Jie, H. Kang, Y. Zhang, S. Guo, H. Ruan, Y. Zhao, Z. Cao, T. Li, *Acta Mater.* **2017**, 124, 143.
- [7] Q. Ding, Y. Zhang, X. Chen, X. Fu, D. Chen, S. Chen, L. Gu, F. Wei, H. Bei, Y. Gao, M. Wen, J. Li, Z. Zhang, T. Zhu, R. O. Ritchie, Q. Yu, *Nature* **2019**, 574, 223.
- [8] Z. Lei, X. Liu, Y. Wu, H. Wang, S. Jiang, S. Wang, X. Hui, Y. Wu, B. Gault, P. Kontis, D. Raabe, L. Gu, Q. Zhang, H. Chen, H. Wang, J. Liu, K. An, Q. Zeng, T. Nieh, Z. Lu, *Nature* **2018**, 563, 546.
- [9] T. Yang, Y. L. Zhao, Y. Tong, Z. B. Jiao, J. Wei, J. X. Cai, X. D. Han, D. Chen, A. Hu, J. J. Kai, K. Lu, Y. Liu, C. T. Liu, *Science* **2018**, 362, 933.
- [10] S. H. Joo, J. W. Bae, W. Y. Park, Y. Shimada, T. Wada, H. S. Kim, A. Takeuchi, T. J. Konno, H. Kato, I. V. Okulov, *Adv. Mater.* **2020**, 32, 1906160.
- [11] O. El-Atwani, N. Li, M. Li, A. Devaraj, J. Baldwin, M. M. Schneider, D. Sobieraj, J. S. Wrobel, D. Nguyen-Manh, S. A. Maloy, E. Martinez, *Sci. Adv.* **2019**, 5, eaav2002.
- [12] Y. Zhang, *High-Entropy Materials, A Brief Introduction*, Springer, Berlin, Germany **2019**.
- [13] L. Jiang, Y. P. Lu, M. Song, C. Lu, K. Sun, Z. Q. Cao, T. M. Wang, F. Gao, L. M. Wang, *Scr. Mater.* **2019**, 165, 128.
- [14] H. L. Huang, Y. Wu, J. Y. He, H. Wang, X. J. Liu, K. An, W. Wu, Z. P. Lu, *Adv. Mater.* **2017**, 29, 1701678.
- [15] S. Wei, F. He, C. C. Tasan, *J. Mater. Res.* **2018**, 33, 2924.
- [16] Z. Li, F. Körmann, B. Grabowski, J. Neugebauer, D. Raabe, *Acta Mater.* **2017**, 136, 262.
- [17] C. L. Tracy, S. Park, D. R. Rittman, S. J. Zinkle, H. Bei, M. Lang, R. C. Ewing, W. L. Mao, *Nat. Commun.* **2017**, 8, 15634.
- [18] F. Zhang, Y. Wu, H. Lou, Z. Zeng, V. B. Prakapenka, E. Greenberg, Y. Ren, J. Yan, J. S. Okasinski, X. Liu, Y. Liu, Q. Zeng, Z. Lu, *Nat. Commun.* **2017**, 8, 15687.
- [19] E. Huang, C. Lin, J. Jain, S. R. Shieh, C. Wang, Y. Chuang, Y. Liao, D. Zhang, T. Huang, T. Lam, W. Woo, S. Y. Lee, *Mater. Today Commun.* **2018**, 14, 10.
- [20] C. Wang, C. L. Tracy, S. Park, J. Liu, F. Ke, F. Zhang, T. Yang, S. Xia, C. Li, Y. Wang, Y. Zhang, W. L. Mao, R. C. Ewing, *Appl. Phys. Lett.* **2019**, 114, 091902.
- [21] B. Cheng, F. Zhang, H. Lou, X. Chen, P. K. Liaw, J. Yan, Z. Zeng, Y. Ding, Q. Zeng, *Scr. Mater.* **2019**, 161, 88.
- [22] A. S. Ahmad, Y. Su, S. Y. Liu, K. Ståhl, Y. D. Wu, X. D. Hui, U. Ruett, O. Gutowski, K. Glazyrin, H. P. Liermann, H. Franz, H. Wang, X. D. Wang, Q. P. Cao, D. X. Zhang, J. Z. Jiang, *J. Appl. Phys.* **2017**, 121, 235901.
- [23] C. Niu, C. R. LaRosa, J. Miao, M. J. Mills, M. Ghazisaeidi, *Nat. Commun.* **2018**, 9, 1363.
- [24] L. J. Santodonato, P. K. Liaw, R. R. Unocic, H. Bei, J. R. Morris, *Nat. Commun.* **2018**, 9, 4520.
- [25] L. K. Béland, Y. N. Osetsky, R. E. Stoller, *NPJ Comput. Mater.* **2016**, 2, 16007.
- [26] R. E. Stoller, A. Tamm, L. K. Béland, G. D. Samolyuk, G. M. Stocks, A. Caro, L. V. Slipchenko, Y. N. Osetsky, A. Aabloo, M. Klintonberg, Y. Wang, *J. Chem. Theory Comput.* **2016**, 12, 2871.
- [27] J. Du, Z. Wu, E. Fu, Y. Liang, X. Wang, P. Wang, K. Yu, X. Ding, M. Li, M. Kirk, *Sci. Technol. Adv. Mat.* **2018**, 19, 212.
- [28] J. Li, D. Y. Xie, S. Xue, C. Fan, Y. Chen, H. Wang, J. Wang, X. Zhang, *Acta Mater.* **2018**, 151, 395.
- [29] Y. Chen, H. Wang, M. A. Kirk, M. Li, J. Wang, X. Zhang, *Scr. Mater.* **2017**, 130, 37.
- [30] J. Wang, N. Li, O. Anderoglu, X. Zhang, A. Misra, J. Y. Huang, J. P. Hirth, *Acta Mater.* **2010**, 58, 2262.
- [31] B. Wu, Z. Xie, J. Huang, J. Lin, Y. Yang, L. Jiang, J. Huang, G. Ye, C. Zhao, S. Yang, B. Sa, *Intermetallics* **2018**, 93, 40.
- [32] O. El-Atwani, J. A. Hinks, G. Greaves, J. P. Allain, S. A. Maloy, *Mater. Res. Lett.* **2017**, 5, 343.
- [33] D. C. Bufford, F. F. Abdeljawad, S. M. Foiles, K. Hattar, *Appl. Phys. Lett.* **2015**, 107, 191901.
- [34] V. Siva, S. S. Sahu, D. P. Datta, P. C. Pradhan, M. Nayak, V. Solanki, D. Topwal, K. Senapati, P. K. Sahoo, *J. Alloy Compd.* **2016**, 680, 722.
- [35] X. T. Zu, F. R. Wan, S. Zhu, L. M. Wang, *Physica B* **2004**, 351, 59.
- [36] D. L. Porter, E. L. Wood, *J. Nucl. Mater.* **1979**, 83, 90.
- [37] L. Yuan, D. Ponge, J. Wittig, P. Choi, J. A. Jiménez, D. Raabe, *Acta Mater.* **2012**, 60, 2790.
- [38] G. B. Olson, M. A. Cohen, *Metall. Trans. A* **1976**, 7, 1897.
- [39] L. Kaufman, M. A. Cohen, *Inst. Metals Monograph* **1956**, 18, 187.
- [40] D. Raabe, S. Sandlöbes, J. Millán, D. Ponge, H. Assadi, M. Herbig, P. P. Choi, *Acta Mater.* **2013**, 61, 6132.
- [41] B. Li, X. M. Zhang, P. C. Clapp, J. A. Rifkin, *J. Appl. Phys.* **2004**, 95, 1698.
- [42] N. C. Law, D. V. Edmonds, *Metall. Trans. A* **1980**, 11, 33.
- [43] D. Raabe, S. Sandlöbes, J. Millán, D. Ponge, H. Assadi, M. Herbig, P. P. Choi, *Acta Mater.* **2013**, 61, 6132.
- [44] Y. Zhang, M. A. Tunes, M. L. Crespillo, F. Zhang, W. L. Boldman, P. D. Rack, L. Jiang, C. Xu, G. Greaves, S. E. Donnelly, L. Wang, W. J. Weber, *Nanotechnology* **2019**, 30, 294004.
- [45] Y. Zhang, M. L. Crespillo, H. Xue, K. Jin, C. H. Chen, C. L. Fontana, J. T. Graham, W. J. Weber, *Nucl. Instrum. Methods Phys. Res.* **2014**, 338, 19.
- [46] W. J. Weber, Y. Zhang, *Curr. Opin. Solid State Mater. Sci.* **2019**, 23, 100757.
- [47] G. Kresse, J. Furthmüller, *Phys. Rev. B* **1996**, 54, 11169.
- [48] P. E. Blochl, *Phys. Rev. B* **1994**, 50, 17953.
- [49] J. P. Perdew, K. Burke, M. Ernzerhof, *Phys. Rev. Lett.* **1996**, 77, 3865.
- [50] M. Methfessel, A. T. Paxton, *Phys. Rev. B* **1989**, 40, 3616.